Contents

List of Figures

List of Tables

Chapter 1

Introduction

Photon Activation Analysis (PAA) is one of several analytical techniques used to quantify the elemental composition of material. These techniques may be categorized as either determine atomic concentrations or nuclei in a material. Most attention has been given to activation analysis were the technique focuses on reactions in the nucleus of the atom. The detection limits of each technique are found in Table 1.1.

Table 1.1: Table of Detection Limits

Method	Limit (ppm)
ICP-MS	$10^{-7} \rightarrow 10^{-3}$
ICP-AES	$10^{-4} \rightarrow 1$
AAS	$1 \rightarrow 100$
(μ)PIXE	$(1 \rightarrow 20)0.5 \rightarrow 5$
(S)XRF	$(100 \geq)\ 3 \rightarrow 20$
NAA	$0.01 \rightarrow 10$
PAA	$0.01 \rightarrow 100$

1.1 Methods of Determining Atomic Concentration in Material

1.1.1 Inductively Coupled Plasma Mass Spectrometry (ICP-MS)

Inductively coupled plasma mass spectrometry (ICP-MS) is an elemental analytical technique that combines a high-temperature ICP plasma with a mass spectrometer. A sample is introduced into the ICP plasma, typically as an aerosol, where it ionizes the sample's atoms. The ions are then brought into the mass spectrometer and focused by electrostatic lenses in the system. Once in the mass spectrometer, the ions are separated by their mass-to-charge ratio. The most commonly used type of mass spectrometer is the quadrupole mass filter. The ability to filter ions this way allows the ICP-MS to supply isotopic information, since different isotopes of the same element have different masses. Once the ions have been separated by their mass-to-charge ratio, they must then be detected or counted by a suitable detector. A channel electron multiplier (CEM) was used in early ICP-MS instrumentation, however, this open glass cone coated with a semi-conductor has since been replaced with discrete metal dynode type detectors. The ICP-MS system has detection limits that range from 10^7 to 0.001 parts-per-million (ppm).

1.1.2 Inductively Coupled Plasma Atomic Emission Spectroscopy (ICP-AES)

Inductively coupled plasma atomic emission spectroscopy (ICP-AES) is sometimes referred to as ICP-OES, meaning 'optical emission spectrometry'. Similar to ICP-MS, it utilizes the ICP plasma to produce exited atoms and ions that will emit electromagnetic radiation at wavelengths characteristic of a particular element. The concentrations of the elements within a sample can be determined based on the intensity of the emissions. The ICP-AES is composed of a ICP and the optical spectrometer. As with ICP-MS, a liquid or organic sample is injected into the hot plasma torch, where compounds are usually completely dissociated. The excited atoms and ions emit radiation at characteristic lines which are focused onto a diffraction grating and slit system where it is dispersed into its component wavelengths in the optical spectrometer. The photomultiplier tubes previous used to measure the light

intensity have been replaced by an array of semiconductor photodetectors such as solid state charge-coupled devices (CCDs). The intensity of each line is compared to previously measured intensities of known concentrations of the elements in order to calibrate the system. ICP-AES has been used to measure trace metals metal concentrations ranging from 10^4 to 1 ppm.

1.1.3 Atomic Absoprtion Spectrometry (multi-element AAS)

Atomic absorption spectrometry (AAS) is a spectra-analytical procedure used for the determination of elements to within $1 \rightarrow 100$ ppm by using the absorption of optical radiation by the atoms. AAS can be used to determine over 70 different elements in solution, but the technique can only measure one element at a time. In order to analyze an element, a liquid sample must be atomized into a vapor. The most common atomizers are flames and electrothermal graphite tube atomizers. Since AAS basic mode of operation is absorption, as opposed to emission, optical radiation that is characteristic of the element to be determined is passed through the sample vapor. A hollow cathode lamp is the most common radiation source in AAS, and most machines utilize two lamps to cover more elements. The radiation then passes into a monochromator, either a prism or diffraction grating, followed by a slit in order to separate the element-specific radiation from any other radiation emitted by the radiation source. The optical radiation is then transmitted to a photomultiplier detector to convert the light into an electrical current.

1.1.4 Particle-Induced X-ray Emission (PIXE)

Particle-induced X-ray Emission (PIXE) is a non-destructive analytical technique used in determining elemental composition of a material or sample. It has detection limits typically around $0.5 \rightarrow 5$ ppm. The particle beam most often used for PIXE is a positive ion beam. Three types of spectra can be collected using PIXE: X-ray emission spectrum, Rutherford backscattering spectrum, and proton transmission spectrum. The proton beam strikes a sample, which causes inner shell vacancies. The outer shell electrons de-excite to replace, or fill, the inner shell vacancies, emitting radiation in the X-ray portion of the electromagnetic spectrum. The energy of the emitted photon characteristic of the atom. These emissions are detected using

energy-dispersive detectors. Protons in the ion beam will also experience elastic collisions, Rutherford backscattering, with the nucleus of the atom. The backscatter can give composition information on the sample and allow for correction of the X-ray photon loss within the sample. Proton transmission can further provide information about the sample.

1.1.5 X-ray Fluorescence Spectrometry (XRF)

X-ray Fluorescence Spectrometry (XRF) is an analytical technique used for elemental analysis, particularly in the investigation of metals, glass, and ceramics. In XRF, the primary X-Rays are most commonly produced by an X-ray tube and have detection limits around $3 \rightarrow 20$ ppm. However, alternative primary sources include synchrotron radiation, with reported detection limits of 100 ppm or better, can be used. The synchrotron is a large electron accelerator which produces electromagnetic radiation across the whole spectrum, with high spectral purity and high beam intensity. Desired sections of the spectrum can be selected and focused while retaining beam intensity. This beam can then be used as the primary beam in XRF analysis. Once the primary X-rays strike the solid sample, two processes occur, scattering and absorption. Vacancies are created in the orbital shell of the sample atoms as a result of energy absorption and the ejection of an electron. The removal of an electron makes the structure of the atom unstable, and electrons in higher orbitals will de-excite to the lower orbital to fill the vacancy. During the change in orbital, radiation is emitted with energy characteristic of the atom present. This secondary radiation from the sample can be analyzed with two different approaches, energy-dispersive or wavelength-dispersive analysis. In energy-dispersive analysis, various types of solid state detectors are used to collect the incoming X-ray photon, while wavelength-dispersive analysis employs a monochromator and a photomultiplier for detection of a single wavelength of radiation.

1.2 Methods of Determining Nuclei in Material

Nuclei of stable elements can become radioactive when they undergo an inelastic collision that results in the addition or removal of a nucleon or several nucleons from the nucleus. Nuclei are usually left in an unstable state and

will almost instantaneously de-excite into a more stable configuration. This process involves the prompt emission of particles or photons. If the initial nucleus to be activated is denoted by ${}^{A}_{Z}X_N$, the incident radiation particle as a, and the product nuclide and promptly emitted particles are denoted by ${}^{A'}_{Z'}Y_{N'}$ and b respectively, the reaction can be represented by the equation

$$ {}^{A}_{Z}X_N + a \rightarrow {}^{A'}_{Z'}Y_{N'} + b \tag{1.1} $$

or, in the abbreviated form

$$ {}^{A}_{Z}X_N(a,b){}^{A'}_{Z'}Y_{N'}. \tag{1.2} $$

The type of the nuclear reaction depends upon the target nucleus and the nature and energy of the incident radiation. Many of these product radioactive nuclei decay through β and subsequent γ emission. The γ-rays are characteristic of that particular decay process. By precise determination of the γ-ray energies it is usually possible to determine not only which isotopes are present, but from the γ intensities it can be determined exactly how much of the original target nucleus was present and consequently the amount of that element present in the sample. The use of neutrons and photons as the activating radiation particle are outlined below.

1.2.1 Neutron Activation Analysis (NAA)

Neutron activation analysis (NAA) is a non-destructive technique used to measure trace elements in materials with detection limits of $0.01 \rightarrow 10$ ppm. In NAA, the incident radiation particle is a neutron. There are range of different neutron sources available, but only a few that offer the high neutron fluxes useful for NAA. These include reactors and accelerators. Since they have high fluxes ($10^{13}\frac{n}{cm^2 \cdot s}$) of neutrons from uranium fission, nuclear reactors offer the highest available sensitivities for most elements. The sequence of events taking place during the most common type of nuclear reaction for NAA, namely neutron capture (n,γ), is illustrated in Figure 1.1.

Upon irradiation, a neutron is absorbed the target nucleus. The compound nucleus transitions to an excited and unstable state. This unstable nucleus de-excites into a more stable configuration by emitting one or more prompt gamma rays. In most cases, this new configuration tends to be a longer lived radioactive nucleus. The newly formed radioactive nucleus now

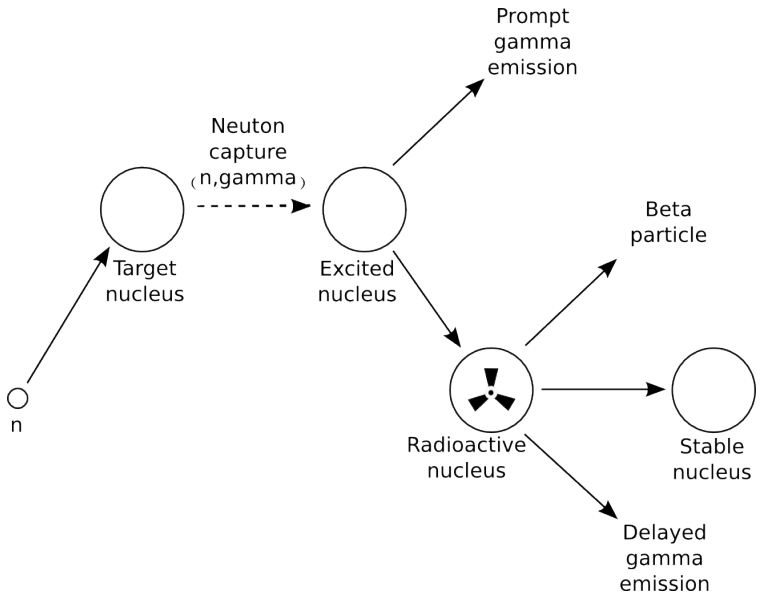

Figure 1.1: Neutron capture process.

decays by the emission of one of more characteristic delayed gamma rays. The half-life of this decay is unique to the radioactive nucleus. An NAA measurement, in principle, falls into two categories: (1) prompt gamma-ray neutron activation analysis (PGNAA), where measurements are taken during the irradiation of a sample, or (2) the more common delayed gamma-ray neutron activation analysis (DGNAA), where measurements follow radioactive decay. There are several types of detectors employed in NAA. Most are designed to detect the emitted radiation. The detectors most commonly used are scintillation type, with radiation sensitive crystals such as thallium-doped sodium iodide (NaI(Tl)), or semiconductor type detectors. Hyper-pure or intrinsic germanium (HpGe) detectors are the semiconductor type most commonly operated for NAA.

1.2.2 Photon Activation Analysis (PAA)

In photon activation analysis (PAA), nuclei in the sample material are excited into radioactive meta-stable states through exposure to high-energy (MeV) photons and has a detection limit of 0.01→100 ppm. The photon source is typically produced by accelerating electrons onto a target layer of

metal with a high atomic number, such as tungsten. The de-acceleration of electrons passing through the target (radiator) produces electromagnetic radiation. Such radiation is referred to as bremsstrahlung radiation. If the bremsstrahlung radiation strikes a sample nucleus and causes results in the removal of a nucleon from the nucleus, the nucleus will more often than not be left in an excited state. The resulting nucleus may be unstable and de-excite by prompt emission of alpha, beta, or gammas. The energy of the emitted γ radiation is usually characteristic of the nuclide. A measurement of the gamma energy can thus be used to identify the nuclear isotope. Similar to NAA, gamma radiation is commonly measured using scintillation type, with radiation sensitive crystals such as thallium-doped sodium iodide (NaI(Tl)), or semiconductor type, such as HpGe detectors.

Concerning the choice of sample that would be activated for PAA study, the main criteria for the activating material was it should allow the testing of coincidence with a high energy and a low energy gamma line. A typical energy spectrum can suffer signal lose in the lower energy ranges do to noise. If a system can trigger on a high energy line in the coincidence measurement, the low energy line can be pulled out of the background noise. From the resources conveniently available, yttrium meet the high and low energy line requirements, and had some additional characteristics that were favorable for testing. That half-life of activated yttrium is 106.63 days. This longer decay time provided a method for decreasing the noise of background decay after irradiation. It is uncertain how long it takes for background to decay after activation. An photon activated material with a long half-life allowed a waiting period for the short lived contaminates to decay away and still have a signal that could be measured. Details of yttrium activation and decay process are described below.

The only natural occurring isotope of yttrium is Y-89. During photon activation of a yttrium foil, a neutron is removed from the nucleus in a ${}^{89}_{39}Y_{50}(\gamma, n){}^{88}_{39}Y_{49}$ reaction. The resulting Y-88 is radioactive with a half-life of 106.6 days. Table 1.2 gives the photon lines for a Y-88 sample. The 898 keV and 1836.1 keV lines have been observed to be the most prevalent with relative intensities of 93.7% and 99.2%. Table 1.3 provides a list of Y-88 photons with the gammas they are in coincidence with. Note that the 898 keV and 1836.1 keV lines are also in coincidence. This coincidence occurs when the 2734.1 keV state, which occurs 94% of the time, makes a transition after 0.7 ps to the 1836.1 keV state, emitting a 898 keV photon. The 1836.1 keV state will decay to the ground state after 0.154 ps and emit a 1836.1 keV

Table 1.2: Y-88 photon lines and intensities.

Energy (keV)	Relative Intensity (%)
850.6	0.065
898.042	93.7
1382.2	0.021
1836.063	99.2
2734.0	0.71
3219.7	0.0070

Table 1.3: Y-88 photons and coincidence gammas.

Energy (keV)	Coincidence gamma (keV)
850.6	898.042, 1836.063, 2734.0
898.042	850.6, **1836.063**
1382.2	1836.063
1836.063	850.6, **898.042**, 1382.2
2734.0	850.6
3219.7	

photon. A diagram of the photon energies and their transitions can be seen in Figure 1.2. The total lifetime of the transitions is less than a picosecond. For our experimental setup, discussed in section 2.3.3, the coincidence timing window was set to 200 ns, so for effective purposes the 898 keV and 1836.1 keV photons are considered in coincidence and will be used for our PAA analysis.

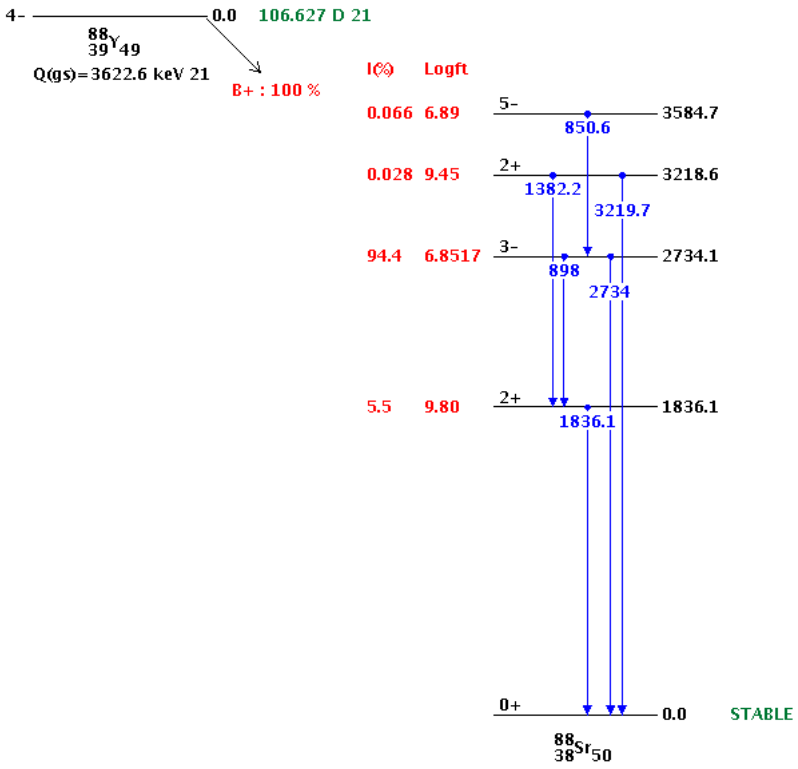

Figure 1.2: Y-88 photon energies and transitions.

Chapter 2

Apparatus

2.1 Yttrium Sample Activation Apparatus

The Idaho Accelerator Center (IAC) operates several electron linear accelerators. In order to photon activate the yttrium foil, the 44 MeV short-pulse LINAC was chosen. Operating the LINAC at an electron beam energy of 22 MeV, the average current was 54.4 μA . Utilizing the following equation:

$$P = E \times I \tag{2.1}$$

the accelerator's power was calculated to be 1.2 kW. The bremsstrahlung converter, used to create the photons, consists of three 0.100" thick tungsten disks separated by approximately 0.150" of water for cooling. The sample activated consisted of a yttrium foil placed between two nickel foils and attached to a polyethylene block. An additional gold foil was inserted between the nickel foil and polyethylene. An illustration of this set-up can be seen in Figure 2.1.

2.2 Coincidence Counting Apparatus

2.2.1 Detectors

HpGe Detector

A high-purity germanium (HpGe) detector is the first of two detectors used in for our coincidence set-up. These detectors employ a germanium semi-

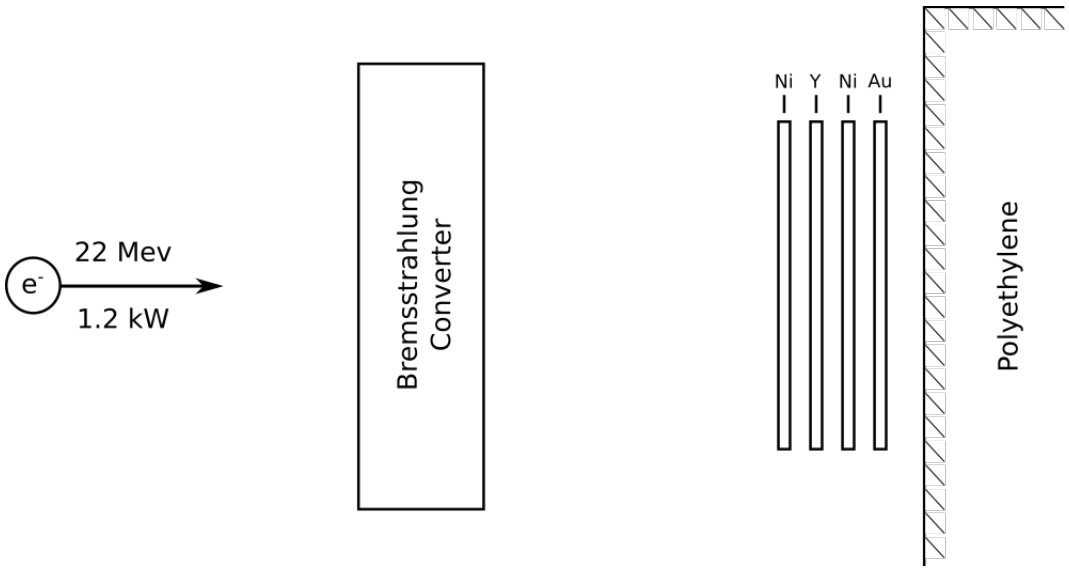

Figure 2.1: Target set-up for photon activation.

conductor to measure the energy of impinging radiation. In semiconductor detectors, the incident photon's energy is measured by the number of charge carriers set free in the material's valence band and transferred to the conduction band. An equal number of electronic vacancies or "holes" are created in the valance band. Placing the material between two electrodes and applying an electric field will give a measurable pulse. In order to reduce thermal excitations of valence electrons, the detector is cooled to liquid nitrogen temperatures. HpGe detectors have an energy resolution of 1 keV. We used a p-type germanium from Ortec model SGD-GEM-50180P-S with an active crystal diameter of 65 mm. The 4600 V detector bias was controlled by the SMART-INTERFACE computer software. Figure 2.2 shows the detector with a dewar attached that kept the detector cool for at least one week before additional nitrogen was required. A diagram of the detector is shown in Figure **??**.

NaI Detector

The second detector employed in our coincidence set-up was a Sodium Iodide (NaI) detector. NaI detectors are a type of scintillation detector usually coupled to a photomultiplier tube (PMT). The NaI scintillator material is

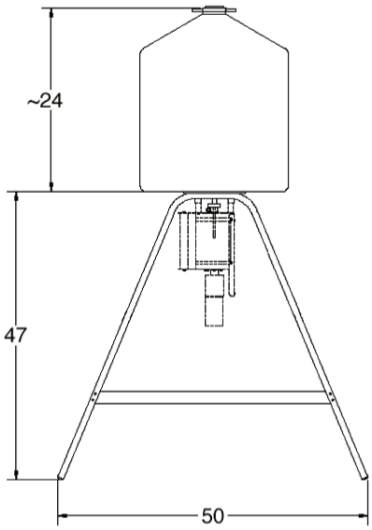

(a) Ortec Detector and Dewar Diagram

(b) Detector B in IAC counting room

Figure 2.2: HpGe Detector used for coincidence counting.

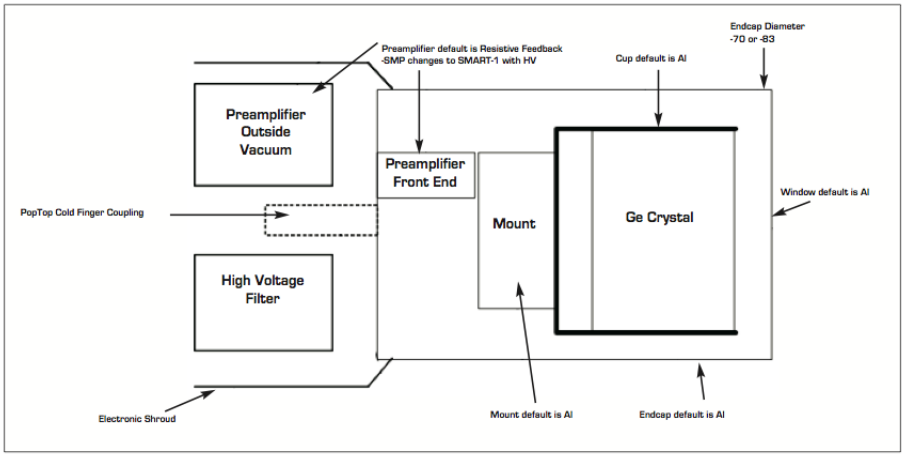

Figure 2.3: HpGe detector internal diagram.

doped with thallium and fluoresces when excited by ionizing radiation. The thallium is used to increase the probability for photon emission. The emitted light strikes a photocathode, releasing at most one photoelectron per photon. The ejected electron is accelerated towards a system of dynodes by an electric field. Additional electrons are knocked off each stage of the dynode as a result of the applied electric field resulting in a measurable signal that is collected at the anode and coupled to a coaxial BNC output connector. We used a Bicron model 3M3/3 detector with a 3×3 inch crystal. The PMT voltage was set at -1000 V. A picture of the detector and its diagram can be seen on Figures 2.4 and 2.5.

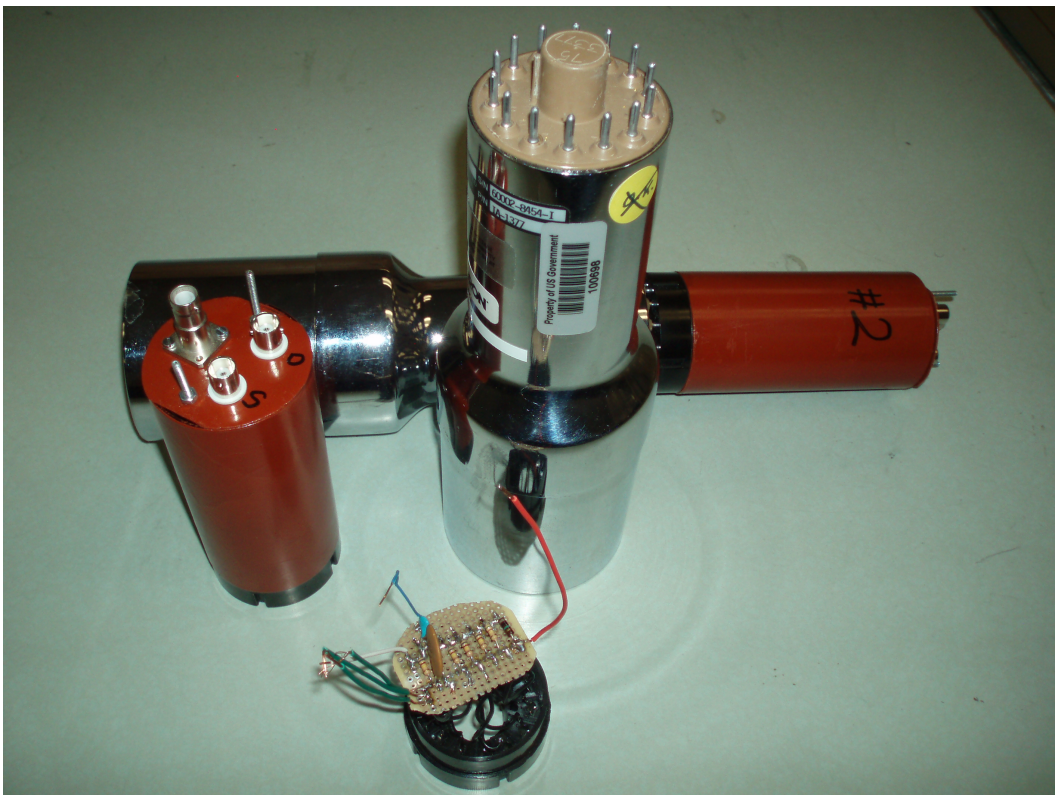

Figure 2.4: Sodium Iodid (NaI) detector and parts.

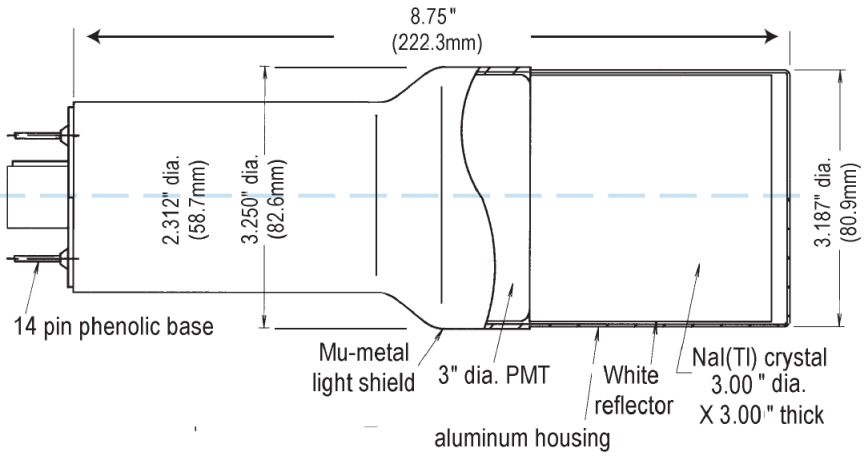

Figure 2.5: NaI detector internal diagram.

Set-Up Geometry

Samples were positioned on top of polyethylene blocks. Polyethylene replaced cement blocks to reduce the background from the cement blocks. The HpGe detector was suspended from a dewar 9.5 cm above the sample. The NaI detector is perpendicular to the HpGe detector and 6.7 cm from the sample. The NaI detector was shielded using two standard ($2 \times 4 \times 8$ inch) Pb bricks. A drawing of the apparatus is shown in Figure 2.6.

2.3 Signal Processing

2.3.1 Analog Output

As seen in the HpGe detector diagram Figure **??**, the charge carriers from the crystal are sent directly to a preamplifier, which converts the charge pulse from the detector to a voltage. This positive voltage signal has a rise time 8 microseconds and a decay time of 60-80 microseconds with an amplitude of 40 mV as shown in Figure 2.7. The signal is next sent to a post amplifier that provides a voltage gain to bring the pulse amplitude to 1.75 V where it can more conveniently be processed. The NaI detector PMT output is

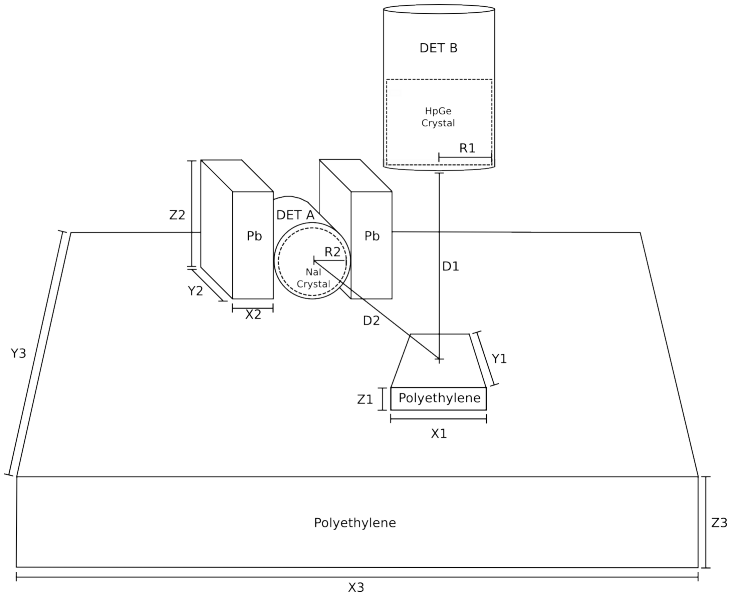

(a) Set-up geometry. The following dimensions were used: x1=7.7cm, y1=9.2cm, z1=2.5cm; x2=5.08cm, y2=20.32cm, z2=10.16cm; x3=61cm, y3=60.5cm, z3=41cm; R1=3.25cm, R2=3.81cm

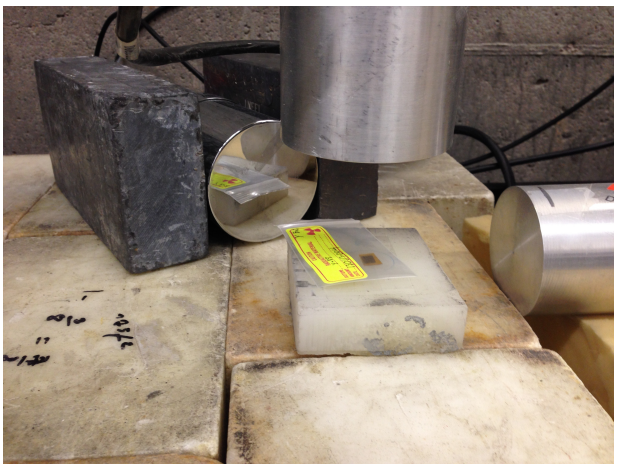

(b) Picture demonstrating sample placement with detectors.

Figure 2.6: Detector set-up and geometry.

shown in Figure 2.8. In contrast to the HpGe signal, the negative voltage NaI signal has a pulse width of 2-3 microseconds and an amplitude between 5 and 10 mV. An inverting amplifier was used to convert the signal to a positive amplitude and broaden the pulse with a gradually rounded maximum peak amplitude of 640 mV. The signal is also more symmetric. The amplified signal can be seen alongside the HpGe amplified signal in Figure 2.8.

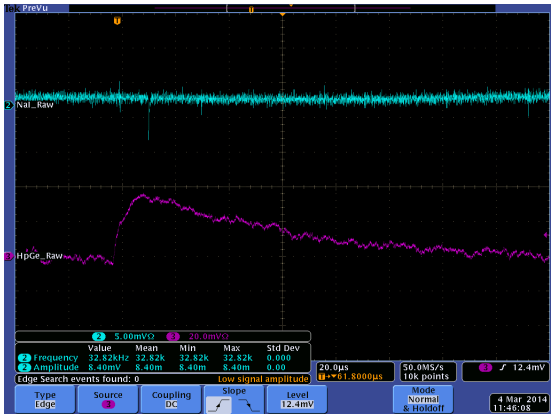

Figure 2.7: NaI and HpGe detector ouput signals before amplification.

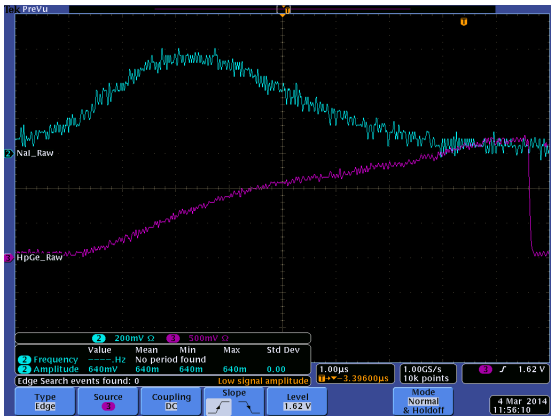

Figure 2.8: NaI and HpGe detector ouput signals after amplification.

2.3.2 Analog Amplification

Figure 2.9 is a diagram of the modules used for the coincidence experiment. Detector B is positioned directly above the source and corresponds to our HpGe detector as mentioned in the set-up geometry section above. The pre-amplified signal of the HpGe detector is post amplified by an ORTEC 673 Spectroscopy Amplifier. The adjustable controls where set to the following values: The Spec-Amp course grain was $\times 20$, the fine grain dial was set to $\times 1.04$ for an overall gain of $\times 20.8$, and the sharpening time to 0.25sec. The BLR switch was in the auto position and the input switch in the positive position. The time variant gated integrator (GI) output from the Spec Amp goes to a Peak Sensing Analog-to-Digital Converter (PADC). The unipolar (UNI) output continues to a Constant Fraction Discriminator (CFD). A NaI detector, Detector A, is shown in Figure 2.9. The NaI detector's analog signal also passes through a post amplifier. We used an Ortec 855 Dual Spectroscopy Amplifier in our set-up. The course gain dial was set to $\times 20$ and the fine gain dial was set to $\times 8.98$ for an overall gain of $\times 179.6$. The outgoing signals were sent from the BI output to a CFD and the UNI output to the PADC.

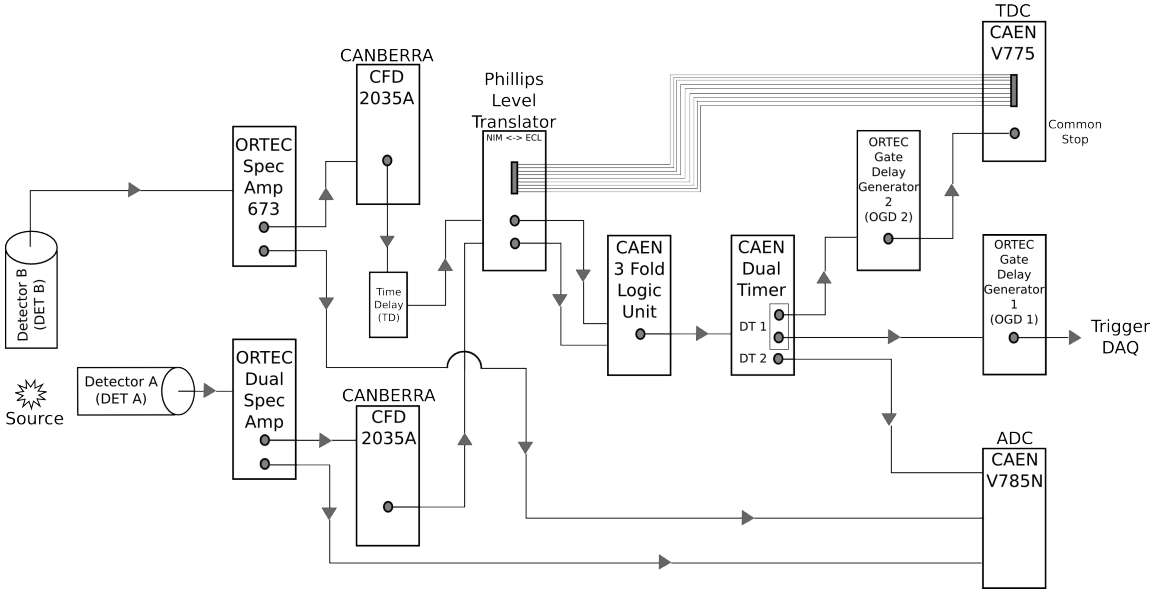

Figure 2.9: Diagram of the modules used for coincidence counting.

2.3.3 Discrimination

For our experiment we used two Canberra 2035A Constant Fraction Timing SCA which performed both energy and timing analysis on post amplified analog pulses. The amplitude of the analog signal is typically proportional to the energy a photon deposits in the detector. Low energy background events are reduced using the discriminator. Both CFD modules where set to accept 60 keV photons or greater. The output logic pulse from this constant fraction discriminator occurs at the same point in the rise of input pulse. To accomplish this, the analog pulse into the discriminator is superimposed onto a copy of that input that has been inverted, attenuated, and offset in time. Adding the two signals yields a bipolar signal. A timing discriminator triggers on the zero-crossing of the signal, producing an output logic pulse. After the CFD, one pulse, with a pulse width of 20 ns, went straight to the a time-to-digital converter (TDC start). A copy of that same pulse went to two gate generators that where used to increase the pulse widths to 100 ns. This increase in the width of the logic pulse corresponds to a 200 ns timing window for coincidence events. In other words, a coincidence is thought to exist if the two output signals occur within 200 seconds of each other.

2.3.4 DAQ Readout Timing

The output of the coincidence logic unit is used to trigger the data acquisition system. The trigger was sent into a CAEN Dual Timer with multiple outputs. One output was given a fixed delay (tstop) with an ORTEC Gate Delay Generator before going to the common stop of the TDC. A second timed pulse, one microsecond wide, was sent to the PADC gate. The analog output from the post amplifiers is delayed in time. This delay was of sufficient length that the amplified analog output was in time with the coincidence logic pulse used start a measurement in the PADC. A copy of that same timed pulse went through a separate gate delay of ttrig and used to signal the DAQ that data was ready to be readout of the VME modules. The trigger was delayed to allow time for the DAQ to convert the analog signals to digital signals. A diagram of these signals, their widths, and their timing can be seen in Figure 2.10.

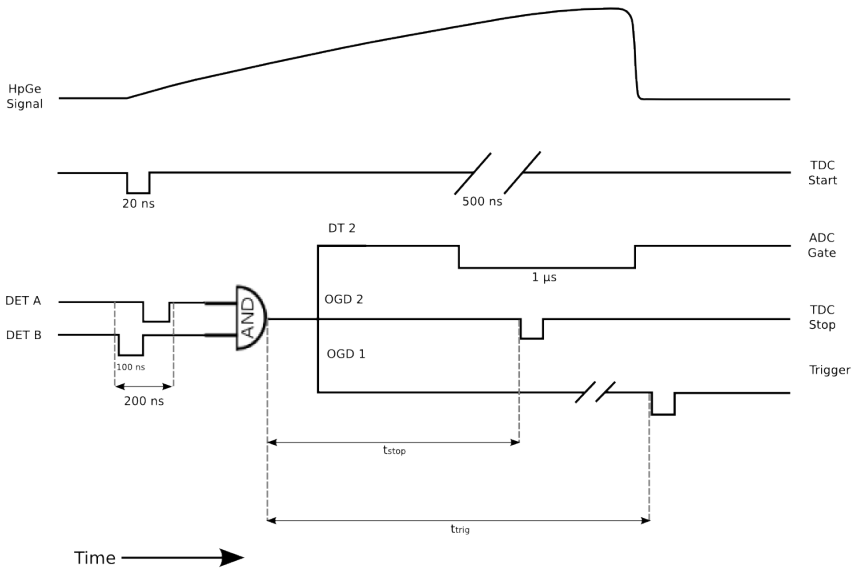

Figure 2.10: Timing Diagram: t_{stop}=600 ns, t_{trig}=13 μs

2.3.5 Coincidence Timing Electronics

A false coincidence background can be suppressed further by requiring simultaneous signals from both detectors. The 20 ns wide logic pulses produced by the CFD are sent to a time-to-digital converter (TDC) and to a logic unit, after their width has been increase to 100 ns as shown in Figure 2.10. The logic unit will compare the timing pulses in an AND gate that only provides output if the two pulses are within a 200 nanosecond window. The coincidence output is used to open a linear gate that signals the PADC to look for a peak within a 1 μs window. Figure 2.11 is a plot of the time difference between the two detector pulses thought to be in coincidence. It shows the expected timing window of $\pm$100 ns. We estimate the probability of having an false coincidence by dividing the number of accidental background event using the number of real coincidence events. The probability of an accidental event was approximately 10.19% for a best case scenario and approximately 24.81% for a worst case scenario.

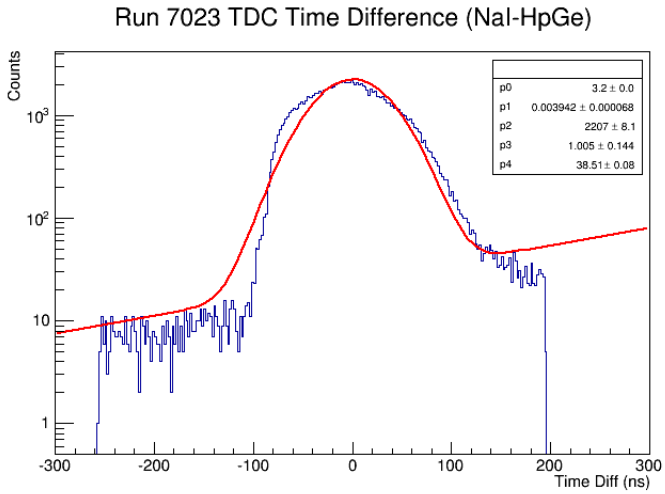

Figure 2.11: Time difference between the NaI detector and the HpGe detector.

Table 2.1: Ba-133 Photon Energies.

Ba-133 Coincidence Photon Energies (keV)	HpGe Energies Before Calibration (keV)
80.9971	220.9 ± 1.81
276.3997	546.6 ± 1.87
302.8510	590.5 ± 1.67
356.0134	678.9 ± 1.52
383.8480	725.1 ± 1.71

2.4 Calibrating Detectors

The detectors are calibrated using standard sources of Cs-137, Co-60, Na-22, Ba-133, and Mn-54. The certificates for these sources along with their coincidence photon energies are be located in Appendix X. Each source was counted in singles mode until the number of events had exceeded 100,000. The mean and sigma of each energy peak was recorded and these values along with the known photon energies where fit to a linear function. Table 2.1 gives Ba-133 known energies in column 1 along with an example of the energies before calibration given by the HpGe detector. The parameters of the fit where applied to calibrate the detectors. Figure 2.12 shows the Ba-133 energy spectrum before and after the detector was calibrated. The long term variance in detector calibration parameters over the course of experiment and the impact of energy calibration drift is analyzed in sectionXX.YY, "Energy Calibration Systematic Error."

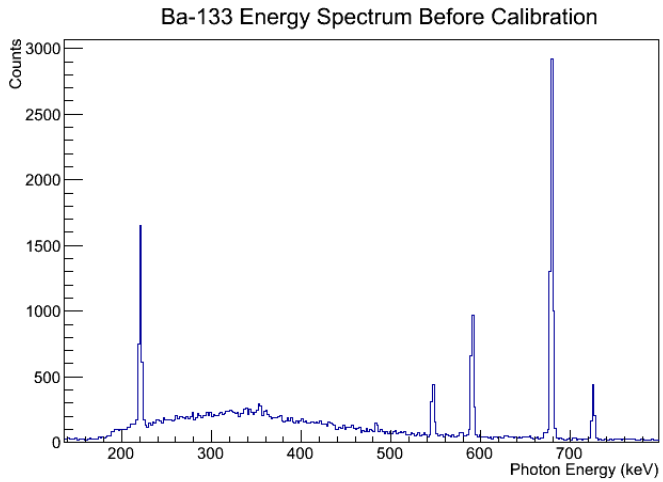

(a) before calibration

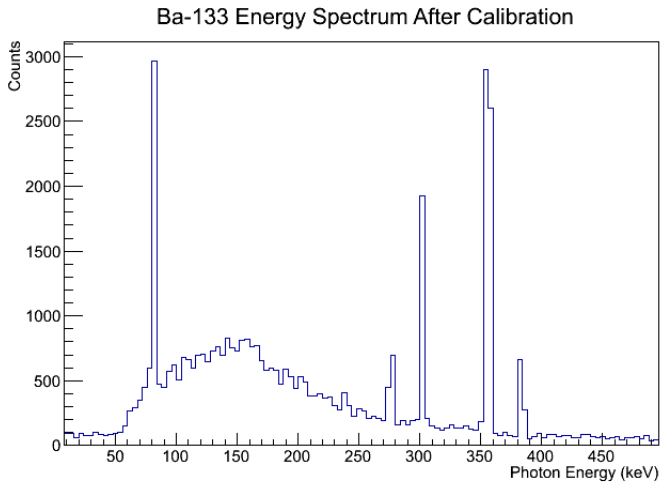

(b) after calibration

Figure 2.12: Ba133 Energy Spectrum.

Chapter 3

Data Analysis

After acquiring the material spectrum using the set-up described in the previous chapter, the 898 keV and 1836.1 keV energy lines are analyzed in order to calculate the using photon activation analysis. It is important to review some terminology use before proceeding with the analysis process. As shown in chapter 2, the module set up included a CAEN 3 Fold Logic Unit. This unit allowed runs to be conducted with an OR gate or an AND gate. Runs that were collected using the OR gate are referred to as singles counts, while runs collected with an AND gate are coincidence counts. It should also be noted that during the analysis of run data the third data point collected, measured 229 days after activation, had significantly smaller activity measured. Upon reviewing calibration runs taken on the same days as yttrium measurements, it was discovered that there was an unknown error affecting the system that particular day. While this third point could be artificially boosted based on the known half-life of yttrium and has been included in some plots and tables presented later, it has been excluded from all data fits related to half-life.

3.1 Analysis of 898 keV and 1836.1 keV Lines

The 898 keV and the 1836.1 keV are the most prevalent photon energy's released in Y-88 decay. Since the total lifetime of the transition states associated with these energies are less than a picosecond, these photons are considered in coincidence for PAA analysis. The following sections describe the methods used to analyze these energy lines using singles and coincidence

counting.

3.1.1 Singles Counting

A Simplistic Method

A simple approach to calculating the detection limit focuses on the amplitude of the energy peaks. Utilizing a data analysis program developed at CERN called ROOT, each peak was fitted to a Gaussian curve. The fit parameters provided the peak amplitude and its associated error and the values can be found in Table 3.1.

Table 3.1: Peak amplitude values used to calculate the half-life of Y-88 for singles counting using a simplistic method.

Run #	Days	$T_{1/2}$	Energy (keV)	Amp
7022	108	1.01	898	1.11421 ± 0.057009
			1836	0.493043 ± 0.040830
7107	159	1.49	898	0.558352 ± 0.044758
			1836	0.265019 ± 0.026870
7235	245	2.30	898	0.434429 ± 0.042097
			1836	0.147541 ± 0.023407

The next step was to look at the need for background removal from the signal. Backgrounds subtraction is an important step to rule out noise or any spectral contribution from materials other than the sample of interest. A simple method to determine the background involves fitting the peak to a line with zero slope. The y-intercept gives the background amplitude. A weighed average of the background was calculated to be 0.0255 ± 0.0206 Hz for the 898 keV line and 0.0072 +/-0.0120 Hz for the 1836.1 keV line. The error on the background supported the assumption that the noise had died away sufficiently to be considered zero. No background was subtracted under the simplistic method for analysis. The peak amplitudes were next fit to the exponential equation:

$$f(t) = e^{(A+Bt)}, \tag{3.1}$$

where A is a constant, B is the slope, and t is the time since activation. Taking the inverse of the fitted slope give the calculated half-life of Y-88.

The half-lives of elements are well studied and known, which meant the calculated half-life provided a check for the values calculated next. Using the fit predators obtained from finding the half-life, it is possible to calculate the initial activity (A_0) of the sample after activation and the additional number of radioactive nuclei (N_0) in the foil. The initial activity is obtained by setting the time equal to zero in the above equation refeq:exp fit. The detector efficiency at measuring the Y-88 energy lines needs to be taken into account. In order to do this, the activity was divided by the calculated efficiency. This will give the absolute activity of the foil. Section XX.XX provides a detailed discussion on how this value was calculated. Using the relationship between activity and the number density:

$$A_0 = \lambda N_0 \tag{3.2}$$

where λ is the decay constant, we can calculate N_0 for t=0. This value used the know half-life of Y-88, rather than the half-life obtained from fits. There should be a value agreement between the values of A_0 and N_0 found using the 898 keV and 1836.1 keV energy lines. The energy line analyzed should not affect the initial number of nuclei activated. The next fit of interest is the signal to noise ratio (SNR). It is desirable to know how long measurements can be taken before the signal is no longer identifiable from the noise, or our SNR is equal to zero. The peak amplitudes are divided by the weighted average background and fit to a line. The linear fit is extrapolated to where it crosses the x-axis the find the time (t_{final}) when measurement is no longer feasible. Table 3.2 lists the values obtained for the signal to noise ratio.

Table 3.2: Signal to Noise Ratio values obtained by dividing the peak amplitude by the background..

Run #	Days	$T_{1/2}$	Energy (keV)	SNR
7022	108	1.01	898	43.69 ± 2.24
			1836	68.48 ± 5.67
7107	159	1.49	898	21.90 ± 1.76
			1836	36.81 ± 3.73
7235	245	2.30	898	17.04 ± 1.65
			1836	20.49 ± 3.25

Since the initial values A0 and N0 have been determined along with a

final time, the decay equations

$$A(t) = A_0 e^{\lambda t} \tag{3.3}$$

$$N(t) = N_0 e^{\lambda t} \tag{3.4}$$

can be utilized to find the final activity and number of radioactive nuclei the can be measured by the set-up. A full summary of the results is located in section XX.XX.

A Rigorous Method

A more complicated method of analysis involves finding the integral of the energy peak by first subtracting the underlying background. The background was determined by fitting the observed window with a function that was a combination of a gaussian curve and a line. The linear fit parameters were entered into a simple program read into ROOT that subtracted the background from the histogram. The remaining signal was integrated to find the area under the peak. The values were fit to an exponential curve to obtain a calculated half-life, activity, and number density using the same approach outlined in the previous section. Figure 3.2 shows this fit. The SNR was calculated by dividing the subtracted signal integral by the integrated area of the background. The data points where subjected to a linear fit and the time t_{final} was extrapolated. After studying the signal to noise plot, the first data point for the singles 898 keV was much smaller and not included in the SNR fit. At the time of measurement, the background noise appears to be larger and decreases the value of the ratio. This could be from contaminants with short half-life in the sample that later decayed away. Only elements with longer half-lives, such as Y-88, remained for the later data points. The backgrounds of the remaining three data points were averaged for the fit. Figure 3.3 plots the SNR values and shows the extrapolated fit.

Looking for agreement between the initial values A_0 and N_0 for the 898 keV and the 1836.1 keV lines shows that they are off by a factor of 2. This more rigorous method fails for single counting. The main contributor to this method failing is believed to be the background. Using the simple method, it was determined earlier that the background noise could be considered consistently zero. The rigorous method could be giving to much weight to the zero background and driving the initial number of nuclei from agreement.

3.1.2 Coincidence Counting

Using our Y-88 source, our set-up allows us to perform runs with the detectors in coincidence (AND mode) or singles (OR mode). Figure 3.1(a) on the left shows the HpGe detector's coincidence events (red) that occurred within a 200 ns timing window. This graph has been overlaid with the same detectors single events (blue). We can see that by having the detectors in coincidence, the noise is reduced and several peaks, which do not have multiple photons in coincidence, are removed.

The coincidence run does not show the two energy peaks associated with Y-88 decay alone. Even though we require coincidence for the system to trigger, there is still noise. These peaks could be Compton events contaminating the coincidence and accidentals. Photons can loss a portion of their energy traveling to the detector. They do not necessarily have to deposit all of their energy into the detector either. The photon can Compton scatter out. It is not possible to tell the difference between a photon that deposited all of its energy from a scattered photon, since the speed of light is so fast and the resolution of the detector so poor. The photons can, however, be distinguished if an energy cut is applied. In order to remove the Compton events and the accidentals, we can require the photon energy to be completely deposited into the detector. This can be achieved by placing an energy cut on the NaI detector around the high energy Y-88 peak in order to pull out the low energy peak and visa versa. This will remove other unwanted photon energies. Figure 3.1(b) is an overlay of the coincidence signal before (blue) and after (red) an energy cut is applied to the companion detector (NaI detector). The noise seen at low energies is greatly reduced after including the cut and improved the signal.

After applying the energy cut to the NaI detector's appropriate energy line, the data was analyzed using the rigorous method prescribed in the previous section. Figure 3.2 shows the integral values and exponential fit results for the rigorous method for singles and coincidence method. It should be noted that for the 898 keV signal to noise fit, the last data point was not included. The extended length of the run, over several days, and activities in the counting room during counting, such as refilling of the nitrogen tank, caused the peak to spread over a larger energy range. This affected the integrated area under the peak as well as the area of the background noise to be larger than expected. The backgrounds of the remaining three points were averaged for determining the SNR. These SNR fits and points can be seen

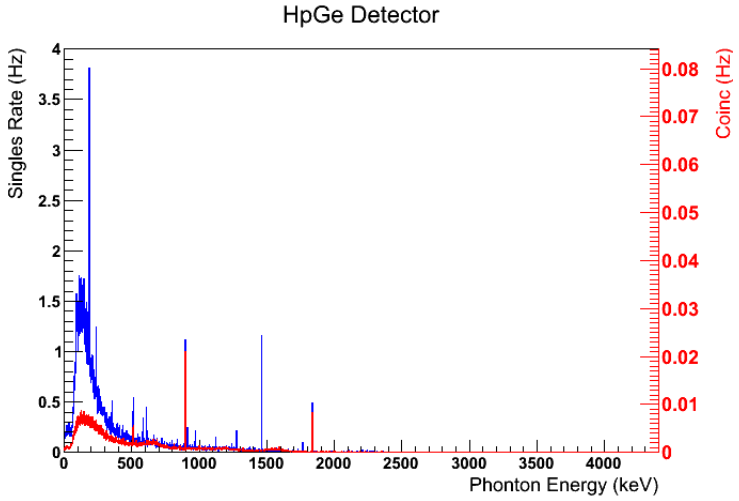

(a) Coincidence Events (red) and Singles Events (blue)

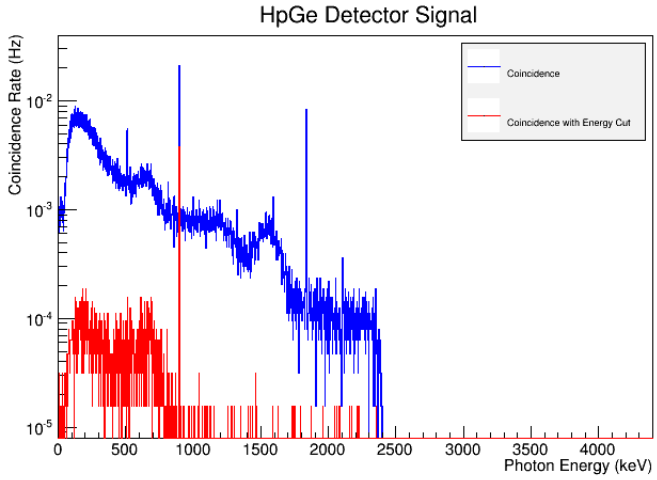

(b) Before energy cut (blue) and after energy cut (red) overlayed

Figure 3.1: Plots of the energy spectrum demostrating noise reduction techniques.

in Figure 3.3 for both singles and coincidence counting. Tables 3.3 and 3.4 give the data used to obtain the fits. A summary of the results are located in section XX.XX.

Table 3.3: Integral values use to calculate the half-life of Y-88.

Days	$T_{1/2}$	Energy (keV)	Integral	Statistical Error	Systematic Error	Systematic Error(No Energy Cut)
108	1.01	898	0.0052	± 2.864e-4	$^{+6.39e-4}_{-1.8e-3}$	$^{+1.86e-4}_{-1.84e-4}$
		1836.1	0.0062	± 3.13e-4	$^{+3.91e-4}_{-2.64e-3}$	$^{+1.14e-4}_{-1.11e-4}$
159	1.49	898	0.0042	± 2.263e-4	$^{+4.43e-4}_{-6.45e-4}$	$^{+8.3e-5}_{-7.82e-5}$
		1836.1	0.0046	±2.37e-4	$^{+4.98e-4}_{-2.87e-3}$	$^{+6.66e-5}_{-7.43e-5}$
229	2.15	898	0.0034	± 2.587e-4	$^{+5.62e-4}_{-1.24e-3}$	$^{+1.41e-4}_{-2.17e-4}$
		1836.1	0.0062	± 4.60e-4	$^{+1.29e-3}_{-6.07e-3}$	$^{+2.39e-4}_{-3.63e-4}$
245	2.30	898	0.0015	± 5.454e-5	$^{+3.68e-4}_{-1.53e-3}$	$^{+1.27e-5}_{-1.47-5}$
		1836.1	0.0016	± 5.63e-5	$^{4.72e-4}_{-1.23e-3}$	$^{+1.20e-4}_{-1.21e-4}$

Table 3.4: Signal to noise ratio values use to calculate t_{final}.

Days	$T_{1/2}$	Energy (keV)	SNR	Statistical Error	Systematic Error
108	1.01	898	46.181	$\pm 4.204(9.10\%)$	$^{+1.653}_{-1.635}$
		1836.1	40.666	$\pm 1.236(3.04\%)$	$^{+0.748}_{-0.728}$
159	1.49	898	37.30	$\pm 1.132(3.03\%)$	$^{+0.739}_{-0.694}$
		1836.1	30.172	$\pm 2.480(8.22\%)$	$^{+0.437}_{-0.489}$
229	2.15	898	30.195	$\pm 2.480(8.21\%)$	$^{+1.253}_{-1.926}$
		1836.1	40.666	$\pm 3.095(7.61\%)$	$^{+1.566}_{-2.379}$
245	2.30	898	37.994	$\pm 4.287(11.28\%)$	$^{+0.322}_{-0.372}$
		1836.1	0.7569	$\pm 0.057(7.57\%)$	$^{+0.0568}_{-0.0572}$

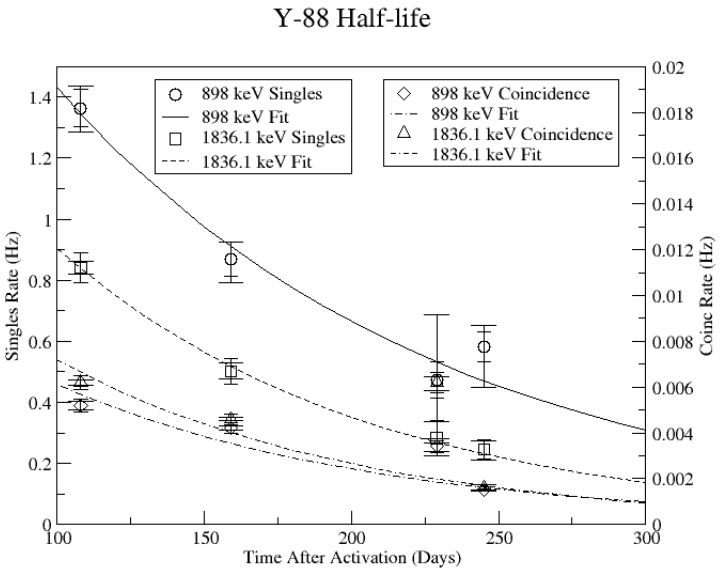

Figure 3.2: Integral values fit to exponential curves for singles and coincidence counting using a rigorous method

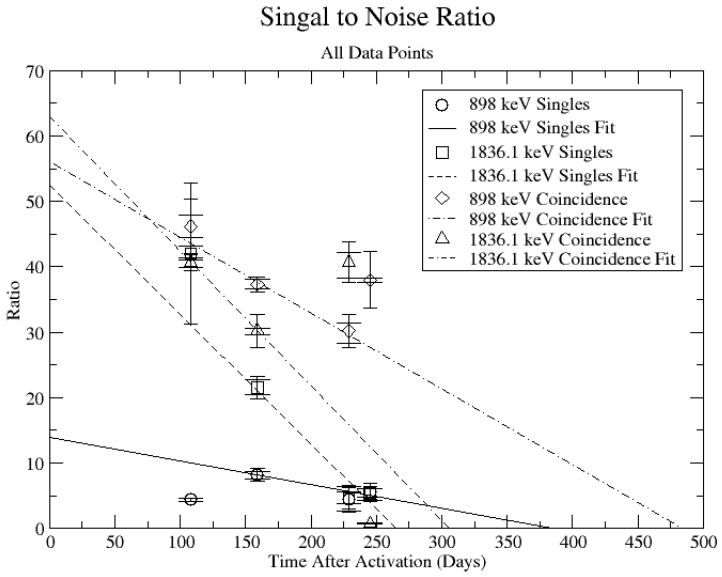

(a) SNR plot showing all data points

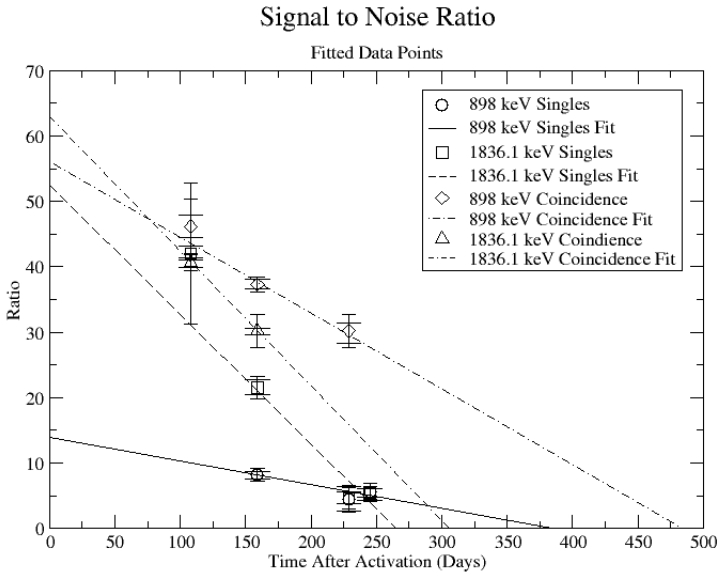

(b) SNR plot showing fitted data points

Figure 3.3: Plots showing the signal to noise ratio with linear fits used to extrapolate time t_{final}.

3.2 Efficiencies

3.2.1 Singles Efficiency

A measurement of the HpGe detectors geometric efficiency for detecting the Y-88 energy lines at 898 keV and 1836.1 keV was performed in order to determine the absolute activity of the sample. The count rate for several sources of known activity was measured by the data acquisition system. Since each sample has decayed since the original calibration by the source vendor, column 4 of Table 3.5 reports the expected rates from each calibrated sample that were calculated using the half life and the known activity of the standard sources. The characteristic energy peaks from each source was fit to a gaussian distribution. The variance from that fit was used to determine the range of integration for the count rate measurement. The integration energy range was selected to include counts over the energy interval from $\bar{E} - (2\sigma + \Delta\sigma)$ to $\bar{E} + (2\sigma + \Delta\sigma)$. The measured rates for each calibrated source using the HpGe detector are listed in column 5. The efficiency given by the ratio of the rates in column 5 to the expected rates in column 4 are shown in column 6 of the same table. The percent efficiency of the standard sources was fit to a exponential curve shown in Figure 3.4(a). The singles efficiency for 898 keV and 1836.1 keV were extrapolated from the exponential equation and are recorded in Table 3.7. This process was repeated for the NaI detector and the results can be seen in Figure 3.4(b) and Tables 3.6 and 3.8.

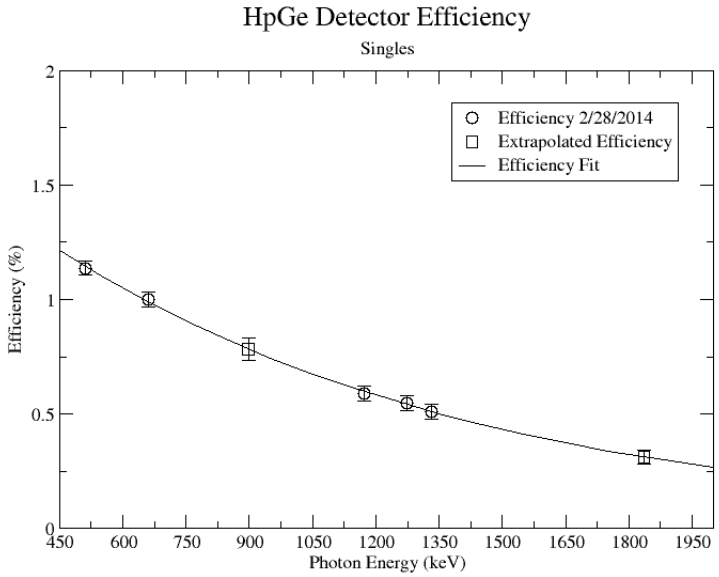

(a) HpGe Detector

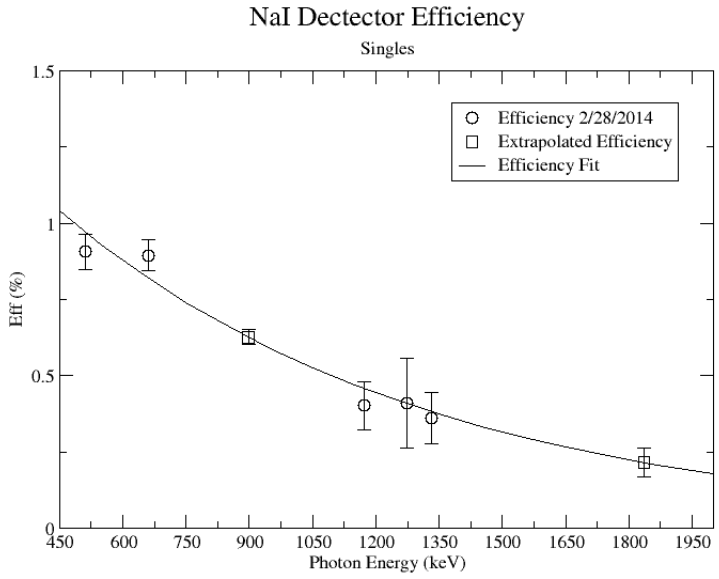

(b) NaI Detector

Figure 3.4: Plots of the detector effeciency for photon energies.

Table 3.5: HpGe Detector Rates and Effeciencies.

Run	Source	Energy	Expected Rate (Hz)	HpGe Det B Rate (ADC 7) (Hz)	HpGe Eff (%)
7027	Na-22	511	1589.218 ± 49.425	18.07 ± 0.111	1.137 ± 0.0317
7025	Cs-137	661.657	2548.03 ± 80.008	25.468± 0.172	0.9995 ± 0.0321
7029	Mn-54	834.848	41.405 ± 1.300	0.485 ± 0.014	1.171 ± 0.0427
7026	Co-60	1173.228	1876.619 ± 58.926	11.03 ± 0.106	0.588 ± 0.0328
7027	Na-22	1274.537	888.264 ± 27.625	4.857 ± 0.034	0.5468 ±0.0319
7026	Co-60	1332.492	1878.167 ± 58.974	9.584 ± 0.023	0.510 ±0.0315

Table 3.6: NaI Detector Rates and Effeciencies.

Run	Source	Energy	Expected Rate (Hz)	NaI Det B Rate (ADC 3) (Hz)	HpGe Eff (%)
7027	Na-22	511	1589.218 ± 49.425	14.393 ± 0.715	0.9057 ± 0.0586
7025	Cs-137	661.657	2548.03 ± 80.008	22.8 ± 0.9154	0.8948 ± 0.0510
7026	Co-60	1173.228	1876.619 ± 58.926	7.529 ± 0.5503	0.4012 ± 0.0796
7027	Na-22	1274.537	888.264 ± 27.625	3.654 ± 0.5266	0.4114 ± 0.1474
7026	Co-60	1332.492	1878.167 ± 58.974	6.784 ± 0.5345	0.3612 ± 0.0848

Table 3.7: HpGe Extrapolated Effeciencies.

Source	Energy	HpGe Eff (%)
Y-88	898	0.7830 ± 0.0471
Y-88	1836.1	0.3119 ± 0.0310

Table 3.8: NaI Extrapolated Effeciencies.

Source	Energy	NaI Eff (%)
Y-88	898	0.6262 ± 0.0246
Y-88	1836.1	0.2158 ± 0.0466

3.2.2 Coincidence Efficiency

Unlike the singles efficiency found above, the efficiency for a coincidence measurement relies on the combined efficiency of both detectors. A known Y-88 source was not available to measure the coincidence activity directly. Instead, the HpGe's geometric efficiency for detecting the Y-88 energy lines at 898 keV and 1836.1 keV was combined with the NaI detectors efficiency for the 1836.1 and 898 keV lines respectively. For example, to obtain the 898 keV coincidence efficiency, the HpGe singles efficiency at this energy line is multiplied by the NaI singles efficiency at the 1836.1 keV line. The uncertainties of the singles efficiency are added in quadrature and the resulting values recorded in column 4 of Table 3.9. The reverse case was applied to find the coincidence efficiency at the 1836.1 keV line and the values are listed in column 4 of Table 3.10.

Table 3.9: HpGe detector efficiency for 898 keV line in coincidence mode.

HpGe Singles 898 keV Eff (%)	NaI Singles 1836.1 keV Eff (%)	HpGe Coincidence Eff (%)
0.7830 ± 0.0471	0.2158 ± 0.0466	0.1690 ± 0.0663

Table 3.10: HpGe detector efficiency for 1836.1 keV line in coincidence mode.

HpGe Singles 1836.1 keV Eff (%)	NaI Singles 898 keV Eff (%)	HpGe Coincidence Eff (%)
0.3119 ±0.0310	0.6262 ± 0.0246	0.1953 ± 0.0396

3.3 Analysis Summary

The following table summaries the results found in this chapter.

Table 3.11: Analysis results for the 898 keV and 1836.1 energy lines. Efficiency has been applied to the results at time t_{final}.

Energy	Trig	$T_{1/2}$ (days)	A_0 (before efficiency) (Hz)	N_0 (before efficiency) (nuclei)	A_0 (after efficiency) (Hz)	N_0
898	sing	127.668 ± 16.8095	2.3901 ± 0.417	3.177e7 ± 5.543e6	305.252 ± 55.1726	
	coin	108.18 ± 4.89	0.0154 ± 0.0003	204958.085 ± 4201.641	9.125 ± 0.633	
1836.1	sing	107.273 ± 17.3321	1.2838 ± 0.1451	1.706e7 ± 1.928e6	411.606 ± 48.2299	
	coin	100.10 ± 4.0	0.0196 ± 0.0004	260440.778 ±5339.036	10.033 ± 0.447	

Chapter 4

Error Analysis

4.1 Energy Window Systematic Error

The signal is measured by subtracting a count rate that is summed over an energy interval. The choice of this integration interval, energy window, is a source of systematic error. In order to calculate the error associated with the energy window, its range was adjusted based on the statistical variance of the background subtracted count rate fit to a gaussian. The integral was measured for window ranges chosen according to an integer interval of the standard deviation $\mu \pm n\sigma$, where n = 3,4,5. The difference between the largest and mid-value was taken as the positive standard deviation, and the lowest was used for the standard deviation negative fluctuation. The resulting errors were divided by the signal to obtain a percent error as shown in column 4 of Tables 4.3, 4.4, 4.5, and 4.6.

4.2 Energy Calibration Systematic Error

Prior to each measurement of the Y-88 sample's activity, the detectors where calibrated using several standard sources with known activity and dominant energy lines. This was accomplished by counting certified samples of Cs-137, Co-60, and Na-22 as well as Ba-133 and Mn-54. The observed mean ADC channel number was correlated with the expected energy line from each of the above sources. The correlation was measured using a standard linear fit algorithm. The linear fit algorithm determines the uncertainty of each fit parameter, the slope and the y-intercept. The effects of this uncertainty on

the signal was analyzed and is referred to as the energy calibration error.

The uncertainty in the energy calibration just before a singles measurement was used to investigate the impact of the calibration on the measured signal for a given energy window of integration. While the singles measurements took less than 10 minutes, the coincidence measurement required more than 24 hours. The long term variance of the energy calibration shown in Figure 4.1 was used to estimate the impact of the energy calibration drift during the coincidence measurements. The fit's y-intercept has a temporal variance corresponding to a relative uncertainty of about 1.865%; the slope is about 0.608%. The effects of this error on the coincidence signal were analyzed. In both cases, the range of the energy widow is held constant while the slope and the y-intercept where adjusted to account for all possible combinations with and without their respective uncertainty. The integral value was recorded after every fit parameter change and the max, min, and mean values were obtained. The difference between the largest and mean value was taken as the positive standard deviation, and the lowest was used for the standard deviation's negative fluctuation. The resulting errors were divided by the signal to obtain a percent error as shown in column 5 of Tables 4.3, 4.4, 4.5, and 4.6.

4.3 Linear Fit Systematic Error

The signal is determine by subtracting the underlying background. A estimate of this background is made by fitting the observed count rate with the function below :

$$f(x) = A \int_{\mu-2\sigma}^{\mu+2\sigma} e^{-\frac{1}{2}\left(\frac{x-\mu}{\sigma}\right)^2} dx + Bx + C. \tag{4.1}$$

The above function contains a Gaussian representing the measured signal and a linear function for the background. The above Figure 4.2 shows the fit applied. The linear fit parameters are used to create a histogram that is subtracted from the raw signal histogram, resulting in a histogram of just a signal. The energy window range used for the fit was adjusted and several fits performed to determine the uncertainty of the fit's slope and y-intercept. This systematic error, based on the fits dependence on the energy window is shown in the table under the column labeled "Linear Fit of Background". The fit parameters where adjusted to determine the maximum and minimum

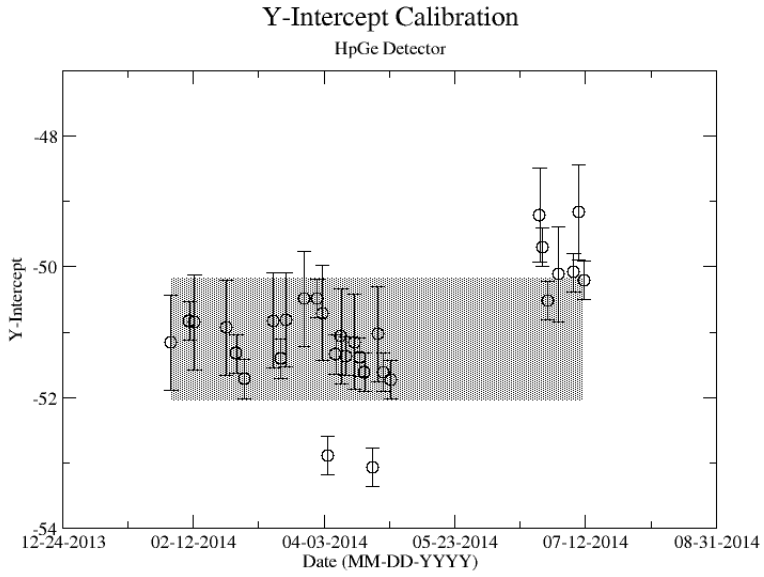

(a) Calibration of the y-intercept

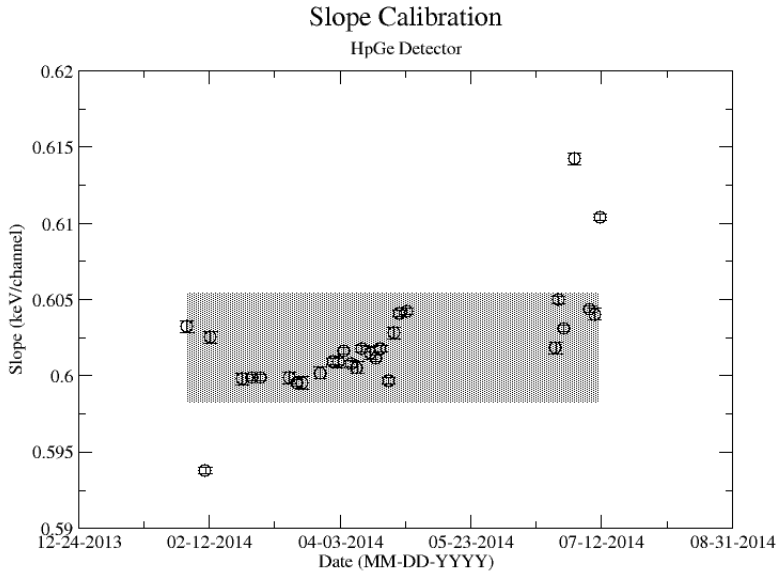

(b) Calibration of the slope

Figure 4.1: Energy calibrations for the HpGe Detector

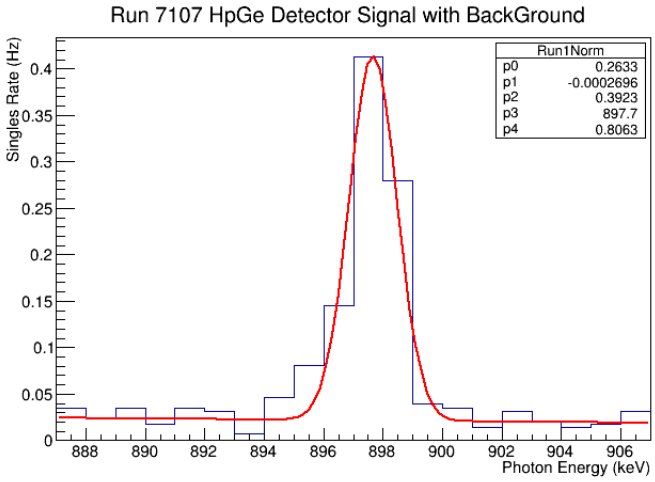

Figure 4.2: A gaussian curve and a line fit to an energy peak.

area of the background. For minimum background area, it was required that the area be positive. The difference between the maximum and unadjusted area value was taken as the positive standard deviation's fluctuation, and the minimum was used for the standard deviation's negative fluctuation. The resulting errors were divided by the signal to obtain a percent error as shown in column 6 of Tables 4.3, 4.4, 4.5, and 4.6.

4.4 Systematic Error of the Coincidence Energy Cut

Figure 4.3 below shows the coincidence measurements made before(blue) and after(red) energy cuts are applied on the NaI signal to reduce the accidental coincidence events and photons that fail to deposit all their energy in the NaI detector due to compton scattering.

To analyze the error association with coincidence counting only, the signal on the NaI detector was fit to a gaussian distribution. The σ of the gaussian fit was used to adjust the energy cut limits. The energy window was set at lower/upper limit$\pm\sigma$. The integral values were recorded for each instance and the difference between the maximum and unadjusted integral values were taken as the positive standard deviation's fluctuation while the minimums

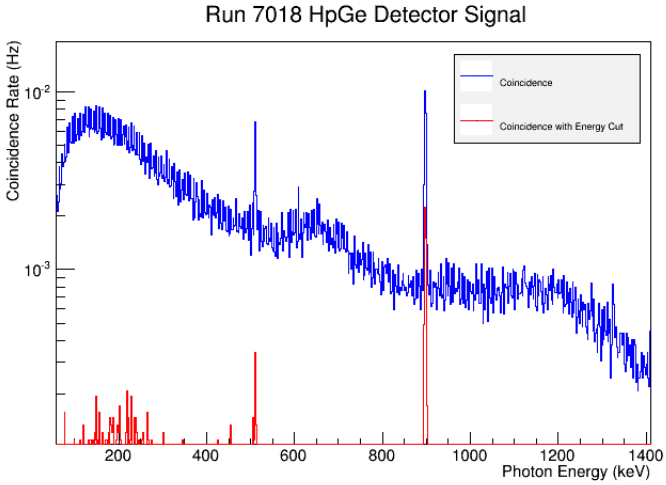

(a) 898 Energy Peak

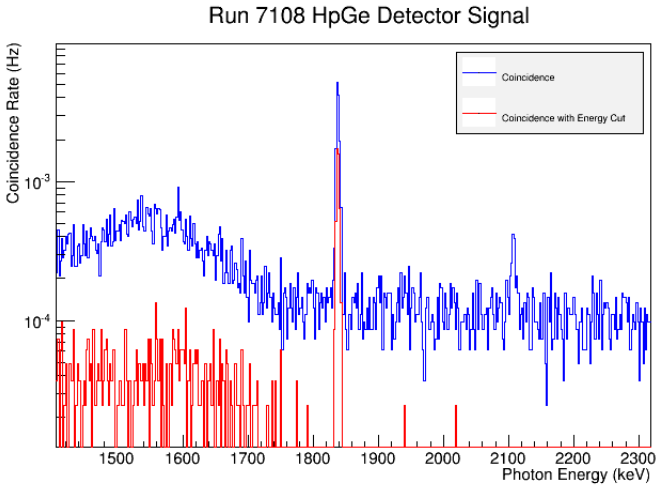

(b) 1836 Energy Peak

Figure 4.3: Plots of the coincidence measurements before (blue) and after (red) energy cuts are applied.

were used for the standard deviation's negative fluctuation. The resulting errors were divided by the coincidence signal to obtain a percent error as shown in column 8 of Tables 4.4 and 4.6. The limited energy resolution of the NaI detector makes this uncertainty the dominant systematic error. If two HpGe detectors are used, then this uncertainty would decrease substantially will be far less than the remaining dominant systematic error; the energy Gaussian integral uncertainty. We report this systematic uncertainty but it is not propagated for the final result in order consider the case of a coincidence apparatus using two HpGe detectors.

4.5 Systematic Error in the SNR

The singles measurement of the 898 keV peak had an initial high background that decays quickly and was more or less constant for singles measurements take 159 days after irradiation. We assumed that this reflected the presence of activated material with half lives longer that 245 days. As a result the background for the last three measurements was averaged and used in the denominator for the SNR. The first singles measurement has a large background due to activated nuclei with short half lives. This background decreased substantially after about 51 days when the next measurement was taken (the half-life of Y-88 is 106.6 days). The singles background near the 1836 keV line was measured to be around 0.5 Hz and fluctuated less over the experiment compared to the background around the 898 peak. The coincidence measurements had such little background, due to the nature of the apparatus, that the background was averaged over the first three measurements for both the 898 and the 1836 peaks separately. The background for the final coincidence measurements was ignored because of the increased noise produced when the detectors nitrogen dewar was filled during the 5 day background measurement. Figure 4.4 shows the background levels during measurement.

The systematic uncertainty of the background was not analyzed and propagated into the final SNR uncertainty. The signal's total systematic error, described above, was used for the final uncertainty. The background's systematic error is being ignored.

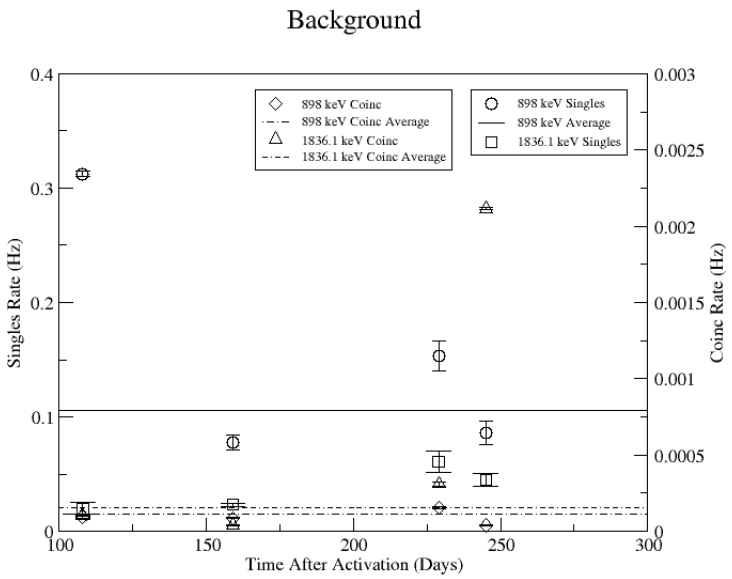

Figure 4.4: The background levels during runs are shown along with the averaged value for both energies.

4.6 Background Contribution to the SNR Error

The analysis of the background uncertainty is described in the above section, "Linear Fit Systematic Error." The background's relative statistical uncertainty shown in column 5 of Tables 4.1 and 4.2 is calculated by varying the integral of the background by the uncertainties from the fit and dividing by the background used for the SNR ratio calculation. Column 6 of Table 4.1 presents the uncertainty of the averaged background as mentioned in the previous section. The variance the coincidence measurement is considerable larger than the individual coincidence measurements. The background in each singles measurement is smaller than the average variance indicating that the individual background measurements could have been made longer to improve their statistical uncertainty.

Table 4.1: 898 keV Background.

Days	$T_{1/2}$	Trig	Background	Linear Fit of Background Error	Statistical Error of Averaged Background
108	1.01	sing	0.3123	±0.801%	N/A
		coin	9.518e-5	$^{+7.73\%}_{-7.45\%}$	±50.01%
159	1.49	sing	0.0777	$^{+8.37\%}_{-8.11\%}$	±5.9%
		coin	8.732e-5	$^{+2.30\%}_{-2.28\%}$	±54.51%
229	2.15	sing	0.1532	$^{+8.36\%}_{-7.96\%}$	±3.0%
		coin	1.554e-4	$^{+5.17\%}_{-5.06\%}$	±30.63%
245	2.30	sing	0.0862	±11.60%	±5.3%
		coin	3.948e-5	$^{+11.24\%}_{-11.06\%}$	±120.57%

Table 4.2: 1836.1 keV Background.

Days	$T_{1/2}$	Trig	Background	Linear Fit of Background Error	Statistical Error
108	1.01	coin	1.037e-4	$^{+2.42\%}_{-2.39\%}$	±951.78%
159	1.49	coin	4.248e-5	$^{+8.06\%}_{-7.88\%}$	±232.34%
229	2.15	coin	3.112e-4	$^{+4.87\%}_{-4.76\%}$	±317.16%
245	2.30	coin	2.114e-3	±0.29%	±46.69%

4.7 Summary

The following tables contain the values found performing error analysis. Tables 4.3 and 4.4 are the calculates errors for the 898 keV line for singles and coincidence counting. The calculates errors for the 1836.1 keV line measured in singles and coincidence mode are located in Tables 4.5 and 4.6.

Table 4.3: Calculated error of 898 kev energy line during singles counting.

Days	$T_{1/2}$	Trig	Energy Window	Energy Calibration	Linear Fit of Background	Gaussian Integration of Signal	Total Sys
108	1.01	sing	$^{+0.367\%}_{-0.660\%}$	$^{+1.026\%}_{-1.83\%}$	$\pm$ 0.183%	$\pm$ 5.132%	$^{+}_{-}$
159	1.49	sing	$^{+0.713\%}_{-3.68\%}$	$^{+0.816\%}_{-2.438\%}$	$^{+0.747\%}_{-0.724\%}$	$\pm$ 6.29%	$^{+}_{-}$
229	2.15	sing	$^{+32.83\%}_{-23.83\%}$	$^{+11.87\%}_{-16.35\%}$	$^{+2.7\%}_{-2.58\%}$	$\pm$ 3.68%	$^{+}_{-}$
245	2.30	sing	$^{+1.19\%}_{-8.28\%}$	$^{+4.24\%}_{-12.0\%}$	$\pm$ 1.72%	$\pm$ 10.68%	$^{+}_{-}$

Table 4.4: Calculated error of 898 kev energy line during coincidence counting.

Days	$T_{1/2}$	Trig	Energy Window	Energy Calibration	Linear Fit of Background	Gaussian Integration of Signal	Coinciden
108	1.01	coin	$^{+0.56\%}_{-0.404\%}$	$\pm 0.31\%$	$^{+0.142\%}_{-0.136\%}$	$\pm 3.46\%$	$^{+10}_{-33}$
159	1.49	coin	$^{+0.405\%}_{-0.048\%}$	$\pm 0.38\%$	$^{+0.048\%}_{-0.047\%}$	$\pm 1.81\%$	$^{+9}_{-1}$
229	2.25	coin	$^{+0.588\%}_{-3.12\%}$	$^{+1.03\%}_{-2.0\%}$	$^{+0.237\%}_{-0.231\%}$	$\pm 3.82\%$	$^{+1}_{-3}$
245	2.30	coin	$^{+0.2\%}_{-0.067\%}$	$^{+0.13\%}_{-0.53\%}$	$^{+0.296\%}_{-0.291\%}$	$\pm 0.719\%$	$^{+2}_{-10}$

Table 4.5: Calculated error of 1836.1 kev energy line during singles counting.

Days	$T_{1/2}$	Trig	Energy Window	Energy Calibration	Linear Fit of Background	Gaussian Integration of Signal	Total Sys
108	1.01	sing	$^{+0.119\%}_{-0.095\%}$	$\pm 0.33\%$	$^{+0.606\%}_{-0.582\%}$	$\pm 2.34\%$	$^{+}_{-}$
159	1.49	sing	$^{+0.199\%}_{-0.798\%}$	$^{+2.81\%}_{-1.42\%}$	$\pm 0.279\%$	$\pm 4.79\%$	$^{+}_{-}$
229	2.15	sing	$^{+10.21\%}_{-7.48\%}$	$^{+4.32\%}_{-8.65\%}$	$^{+3.26\%}_{-3.01\%}$	$^{+11.37\%}_{-11.34\%}$	$^{+}_{-}$
245	2.30	sing	$^{+0.245\%}_{-5.31\%}$	$\pm 1.674\%$	$^{+2.246\%}_{-2.205\%}$	$^{+11.025\%}_{-11.107\%}$	$^{+1}_{-1}$

Table 4.6: Calculated error of 1836.1 kev energy line during coincidence counting.

Days	$T_{1/2}$	Trig	Energy Window	Energy Calibration	Linear Fit of Background	Gaussian Integration of Signal	Coinciden
108	1.01	coin	$^{+0.613\%}_{-0.55\%}$	$^{+0.52\%}_{-0.5\%}$	$\pm 0.04\%$	$\pm 1.45\%$	
159	1.49	coin	$^{+0.435\%}_{-0.196\%}$	$^{+0.261\%}_{-0.804\%}$	$^{+0.074\%}_{-0.073\%}$	$\pm 1.267\%$	
229	2.15	coin	$^{+0.629\%}_{-2.55\%}$	$^{+1.11\%}_{-2.19\%}$	$^{+0.244\%}_{-0.239\%}$	$\pm 3.44\%$	
245	2.30	coin	$^{+0.125\%}_{-0.438\%}$	$\pm 0.188\%$	$\pm 0.386\%$	$\pm 7.5\%$	